Chapter 2
The Large Hadron Collider and the ATLAS Experiment

'Curiouser and curiouser!' cried Alice (she was so much surprised,
that for the moment she quite forgot how to speak good English);
'now I'm opening out like the largest telescope that ever was!
Good-bye, feet!'

Lewis Carroll, Alice's Adventures in Wonderland

Abstract This chapter focuses on the experimental setup of the LHC and the ATLAS experiment. The first part of the chapter introduces the main features that characterize the LHC. The following two sections give a general overview of the different parts of the ATLAS detector and the trigger system. Finally, the last two sections include a brief description of the detector simulation and a summary of the techniques used for object reconstruction, with a special emphasis on jets.

This thesis uses data taken by the ATLAS ("A Toroidal LHC ApparatuS") Experiment [1]. It is one of the experiments at the Large Hadron Collider (LHC) at the *Centre Européen pour la Recherche Nucléaire*, CERN.

The LHC is the highest-energy particle accelerator in the world, and delivers of the order of hundreds of millions of collisions per second. These two ingredients are essential for the physics goals of ATLAS. The first part of this chapter introduces the main features that give the LHC its unprecedented power.

ATLAS is a general-purpose detector composed of a series of sub-detectors, each of which is optimised to perform a different type of measurement. The second part of this chapter will focus on the different sub-components of ATLAS, and on the algorithms used to reconstruct and identify the physics objects used in the analyses that will be presented in this thesis.

2.1 The Large Hadron Collider

The LHC [2] is a particle collider situated at CERN in Geneva, Switzerland. Between 2010 and 2012, it collided proton beams at centre-of-mass energies $\sqrt{s} = 7\,\text{TeV}$ (in

M. Crispín Ortuzar, *High Jet Multiplicity Physics at the LHC*,
Springer Theses, DOI 10.1007/978-3-319-43461-2_2

2010 and 2011) and 8 TeV (in 2012) at four interaction points. It entered a shutdown phase in 2013 and will restart in 2015 at 13 TeV of centre-of-mass energy.

The LHC is a synchrotron 27 km in circumference, housed in the tunnel originally built for the Large Electron-Positron Collider (LEP) between 1984 and 1989. The tunnel crosses the French-Swiss border and lies at an average depth of 100 m underground. Along the circumference are 1232 superconducting dipole magnets kept at 1.9 K which bend the trajectory of the protons.

The LHC has been designed to collide protons and lead nuclei.[1] All the data used in this thesis come from proton-proton collisions. Protons are produced by ionising hydrogen inside a *duoplasmatron*, which generates a plasma of electrons, protons and molecular ions. Protons are then extracted and injected into the first of a series of accelerators in which their energy increases progressively. A schematic of the CERN accelerator complex is shown in Fig. 2.1. Protons reach an energy of 450 GeV before being injected in the LHC in two counter-circulating beams. In 2010 and 2011, each beam was accelerated to up to 3.5 TeV, and in 2012 they reached 4 TeV. The protons are arranged in up to 2808 bunches per beam with a nominal bunch spacing of 25 ns, although for most of 2011 and 2012 the bunch spacing was 50 ns.

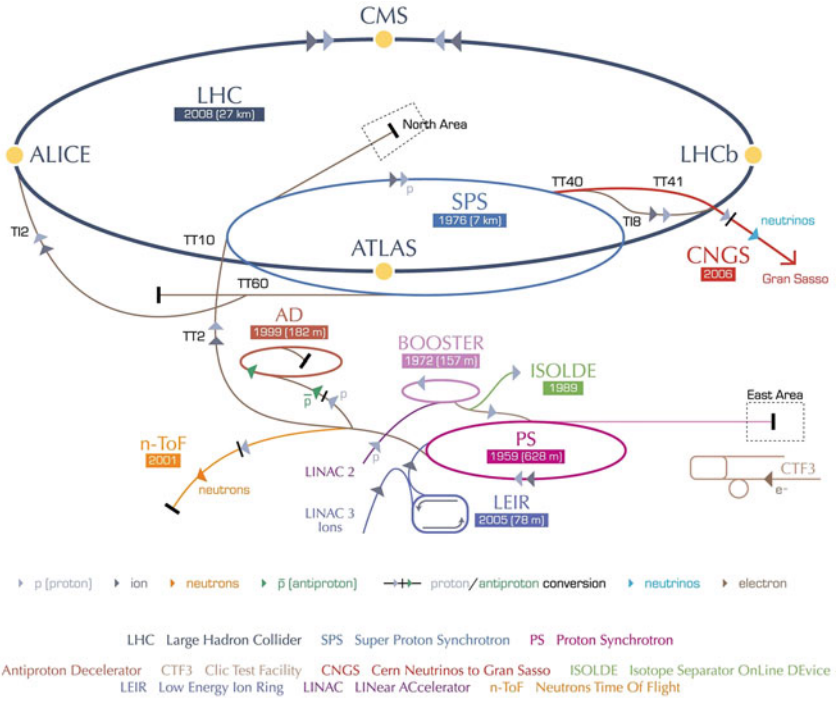

Fig. 2.1 The accelerator complex at CERN (not to scale), including the LHC, its pre-accelerators, and other active facilities

[1] The centre-of-mass energy in this case is 2.76 TeV per nucleon.

The proton beams collide at four interaction points distributed around the ring. The experiments are situated at each of these points to detect and measure the particles produced in the collisions. The ATLAS experiment is one of the two general–purpose detectors, the other one being the Compact Muon Solenoid (CMS) [3]. The main physics goals of the ATLAS collaboration are the study of new physics phenomena at the TeV scale, the discovery of the Higgs boson, and the performance of precision measurements of the Standard Model of particle physics. It is a collaboration of roughly 3000 physicists from all over the world. The other two large experiments installed around the collision points are LHCb, designed to perform heavy-flavour physics measurements, and ALICE, designed for lead-lead collisions.

After the energy, the second most important figure of merit of the LHC is the luminosity. The luminosity $\mathcal{L}$ connects the rate of events $R = \frac{dN}{dt}$ to the cross section σ of a given process:

$$R = \mathcal{L}\sigma. \tag{2.1}$$

The luminosity can be understood as the quantity that measures the ability of the collider to produce the required number of interactions of a particular process. The physics goals of the LHC include searches for rare processes, and therefore require high luminosities. The peak instantaneous luminosity reached in 2012 was $\sim 7 \times 10^{33}\,\mathrm{cm}^{-2}\mathrm{s}^{-1}$. The design luminosity is $\sim 10^{34}\,\mathrm{cm}^{-2}\mathrm{s}^{-1}$, which translates into $\sim$22 simultaneous proton-proton interactions and $\mathcal{O}(1000)$ particles being produced in the central detector region in every bunch crossing [4, 5]. The presence of additional proton-proton interactions in a single measured event is called *pile-up*, and requires careful studies from physics analyses. Pile-up can be *in-time*, if the additional interactions came from the same bunch crossing, or *out-of-time*, if the electronic signals from different collisions overlapped. These conditions are challenging from the perspective of the design of the detectors, which must withstand very high levels of radiation. The properties of the ATLAS detectors will be described in Sect. 2.2.

Integrating the 'instantaneous' luminosity defined above over time gives the 'integrated luminosity', which is directly related to the total number of observed events, and is therefore commonly used to express the size of a dataset. A total integrated luminosity of 5.61 fb^{-1} (7 TeV data) was delivered in 2011, and 23.3 fb^{-1} (of 8 TeV data) in 2012 [6]. A fast selection system is needed to select the small fraction of the data that can be physically recorded and analysed. This system is known as the *trigger*, and will be presented in Sect. 2.3.

2.2 ATLAS Detector Overview

ATLAS has three main subdetectors designed to identify and measure the properties of different types of particles. Its general layout is shown in Fig. 2.2. It follows the conventional layered design, with three main types of sub-detectors (particle tracking detectors, calorimeters and muon detectors), and is nominally forward-backward symmetric with respect to the interaction point. The presence of magnetic fields

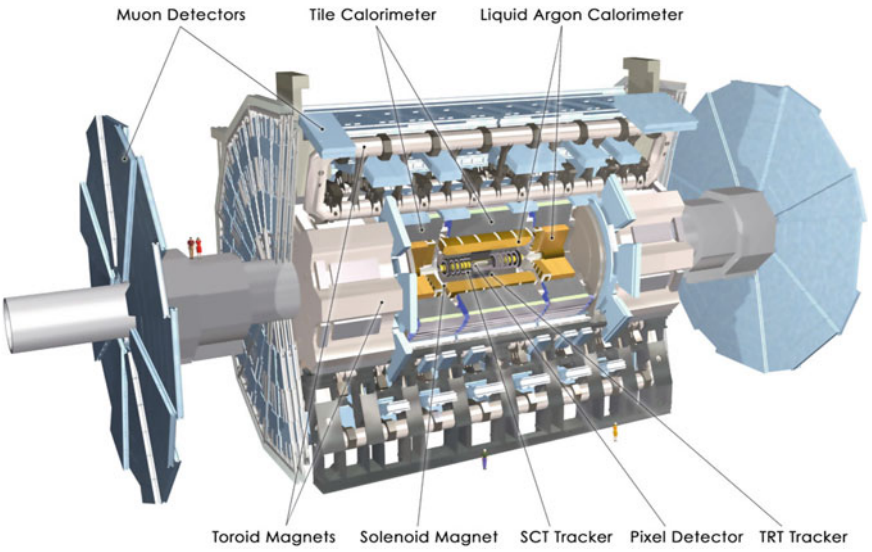

Fig. 2.2 Layout and sub-detectors of the ATLAS detector. The detector is 44 m long and 25 m high, and weighs approximately 7 tonnes. From [7]

permits the measurement of the momenta of charged particles via the curvature of their trajectories; this is the purpose of the solenoid magnet surrounding the tracker and of the toroid magnets interleaved with the muon detectors. All of them are superconducting and cooled by liquid helium to a temperature of 4.5 K.

The **inner detector** (ID) system is located around the interaction point. It consists of a high-resolution pixel detector nearest the beamline, followed by the strip-based semiconductor tracker (SCT) and the transition radiation tracker (TRT). Its main goals are locating the interaction vertex, measuring displaced vertices from long-lived particles and measuring the track momentum with high precision. More details on the ID are given in Sect. 2.2.2. The **calorimeter system** measures the energy and position of electrons, taus, photons and hadrons. There is an electromagnetic calorimeter and a hadronic calorimeter, both of which are described in Sect. 2.2.3. The **muon system** is responsible for triggering on and measuring the muon momentum. High precision chambers are used for precise measurements of muons, and coarser chambers are used for triggering muon events. The muon system is described in Sect. 2.2.4.

The layout and sub-detectors of ATLAS are depicted in Fig. 2.2.

2.2.1 Coordinate System

The coordinate axes used by ATLAS form a right-handed system in which the x-axis points to the centre of the LHC ring, the z-axis follows the beam direction and the y-axis points upwards. The azimuthal angle ϕ is measured around the beampipe, on

the plane perpendicular to it. $\phi = 0$ corresponds to the positive x-axis and ϕ increases clockwise looking into the positive z direction. The polar angle θ is the angle from the z beam axis. It is more common to use instead the pseudorapidity η, defined as $\eta = -\ln\tan(\theta/2)$. The pseudorapidity is an approximation of the physical rapidity Y in the limit when the particle is travelling close to the speed of light. The rapidity is defined as

$$Y = \frac{1}{2}\frac{E + p_z c}{E - p_z c}. \tag{2.2}$$

The pseudorapidity is a common choice of coordinate because the particle flux from the interaction point is approximately constant as a function of η. The pseudorapidity is 0 anywhere in the $z = 0$ plane and tends towards $\pm\infty$ in the forward and backward directions, respectively. The ID provides coverage up to $\eta = \pm 2.5$ (approximately 0.05π rad away from the beampipe) and the calorimeters up to around $\eta = \pm 5$ (approximately 0.004π rad away from the beampipe).

The detector is generally divided in three regions in η: barrel, endcap and forward. The exact η boundaries vary according to the context, but they are typically around $\eta \sim 1.5$ and $\eta \sim 3.2$.

2.2.2 Inner Detector

The inner detector (ID) reconstructs the trajectories, or *tracks*, of electrically charged particles. Tracks can be used for particle identification, to measure particle momentum (in combination with the solenoid magnet), to reconstruct the vertex from which a set of particles originate, and following from this, to measure the distance of a secondary set of tracks from the primary interaction vertex. This last measurement makes it possible to identify jets coming from the decay of a b quark, as most b-hadrons have lifetimes of $\sim$1 ps, which implies decay lengths of $\mathcal{O}$(mm) [8]. Other particles that can be identified via this mechanism include c quarks or τ leptons.

An overview of the ID is shown in Fig. 2.3. Two precision tracking detectors, pixel and SCT, cover the region $|\eta| < 2.5$. The principle of operation relies on the production of free charge carriers in silicon by the incoming particles, with carriers travelling to the electrodes under the influence of an electric field. The energy of the ionising particle can be inferred from the number of electron-hole pairs detected. Semiconductor trackers have very high time and energy resolution, and are small in size compared to gaseous detectors.

The pixel detector consists of a barrel made of concentric cylinders around the beam axis, and two end-cap regions with three disks each. The barrel provides the highest granularity of the ID, with a minimum pixel size of $50 \times 400\,\mu\text{m}^2$. The pixel detector is capable of providing very accurate measurements of the impact parameter of tracks, thus helping detect particles with non-negligible lifetimes such as b-hadrons or τ leptons. The detecting units of the SCT are strips, instead of pixels. They are organised in a similar manner to the pixel detector, with four cylindrical

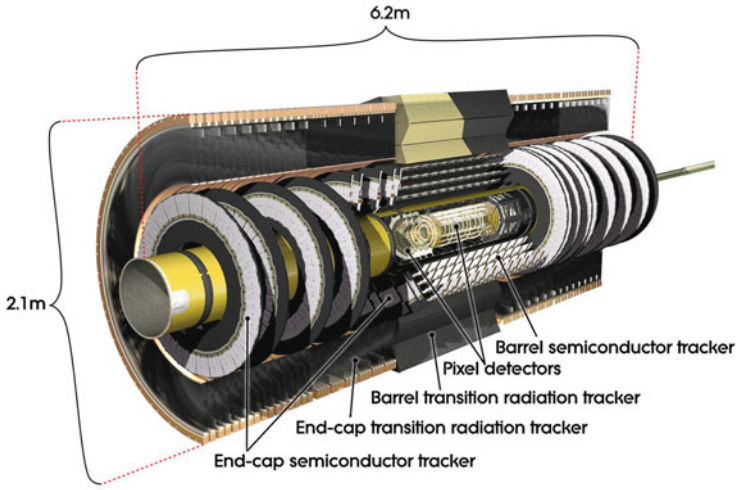

Fig. 2.3 Layout and sub-components of the ATLAS Inner Detector. From [7]

layers in the barrel and nine disks in the two end-cap regions. It uses two sets of strips with a relative rotation of 40 mrad to measure all coordinates. The mean pitch of the strips is approximately 80 μm. The SCT plays an important role in the momentum measurement, as well as the impact parameter and vertex position.

The TRT was designed to extend the tracking measurements to larger radii, as well as to provide electron identification via the detection of transition radiation. The tracking measurement is provided in the $r - \phi$ plane by straw drift tubes filled by a Xe-based gas mixture, which function as ionisation chambers in the proportional regime. The material surrounding the straws consists of multiple layers with different dielectric constants, which triggers the emission of transition radiation by charged particles traversing the medium. The intensity of the radiation is proportional to the Lorentz factor of the incoming particle, which permits the discrimination of ultra-relativistic electrons from other heavier hadronic particles. The straw tubes are situated parallel to the beam axis in the barrel region, and radially in wheels in the end-caps, reaching up to $|\eta| = 2.0$. It has a lower resolution per point compared to the silicon detectors, but provides larger numbers of measurements, and the measured track lengths are longer.

2.2.3 Calorimetry

The ATLAS calorimeters provide a measurement of the energy and momentum of particles, both electrically charged and neutral ones. A layout of the system is shown in Fig. 2.4. The calorimeters cover up to $|\eta| = 4.9$ and combine different techniques to

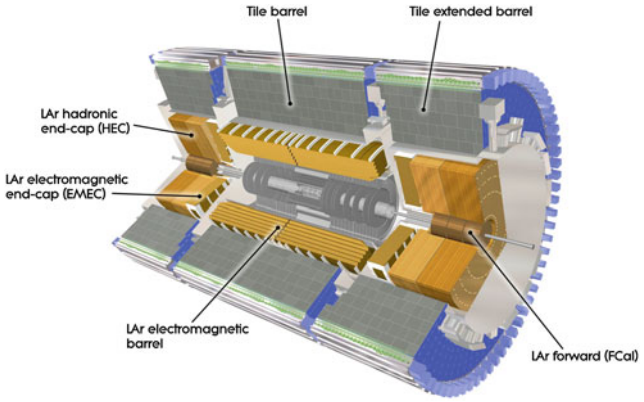

Fig. 2.4 Layout of the ATLAS calorimeter system. From [7]

cover the characteristics of the different physics processes of interest. The distribution of the different calorimeters in ATLAS is as follows. The first layer of calorimetry is formed, in order of increasing rapidity, by the electromagnetic barrel calorimeter ($|\eta| < 1.475$), the electromagnetic end-cap calorimeters (EMEC, covering $1.375 < |\eta| < 3.2$), the hadronic end-cap calorimeters (HEC, $1.5 < |\eta| < 3.2$), and the forward calorimeters (FCal, covering the region $3.1 < |\eta| < 4.9$). The outer layer is formed by the hadronic tile calorimeters, with one central ($|\eta| < 1.0$) and two extended ($0.8 < |\eta| < 1.7$) barrels.

The energy measurement in calorimeters is based on the interaction of the incoming particle with the detector, producing a shower of daughter particles whose energy is deposited in the material, collected and measured. The segmentation of the calorimeter allows one also to obtain information about the direction of the particles and the shape of the shower, which helps with particle identification. In addition, the response from the calorimeters is fast, so they are widely used for triggering.

The ATLAS calorimeters are sampling detectors, which means that the active material providing the signal is different from the medium responsible for absorbing the particle energy.

The electromagnetic calorimeters use liquid argon (LAr) as the active material. LAr is known to be intrinsically radiation hard, as well as have a linear and stable response over time. In addition, they use lead as an absorbing material, with readout electrodes situated in the gaps between the absorbers. They are distributed in an accordion shape, which provides full coverage in ϕ and a fast extraction of the signal. In the central region, where precision measurements are required for electrons and photons, the first layer is finely segmented in η to improve the position determination. The electrodes are etched to obtain projective[2] segments in η and in depth, whereas the segmentation in ϕ is achieved by grouping the signal from the appropriate electrodes.

[2] 'Projective' means in this context that the size of the elements grows proportionally to the distance from the interaction point.

The smallest strips on the first layer are $\Delta\eta \times \Delta\phi \sim 0.003 \times 0.1$ in size, while the two following layers, organised in 'towers' pointing to the interaction point, have a size of $\Delta\eta \times \Delta\phi \sim 0.025 \times 0.025$ or larger.

The hadronic tile calorimeters use scintillator as active material, and steel as the absorber medium. The barrel hadronic calorimeter is divided into three sections (central and extended barrels), composed by wedges of size $\Delta\phi \sim 0.1$ and made of alternating, radially-oriented scintillator tiles and steel plates. The readout fibres are grouped into photomultiplier tubes, providing a projective segmentation in η. To minimise the loss of energy in the gaps between the central and extended barrels, those regions have special steel-scintillator modules. The hadronic end-cap calorimeters suffer harsher radiation conditions, and are therefore based on copper/LAr technology. They consist of two wheels, with $\Delta\eta \times \Delta\phi = 0.1 \times 0.1$ readout cells in the region $|\eta| < 2.5$ and $\Delta\eta \times \Delta\phi = 0.2 \times 0.2$ for the rest. The FCal is split into three modules. The first one is an electromagnetic module with copper as absorber material, and the other two are hadronic modules using tungsten as the absorbing material.

2.2.4 Muon Spectrometer

The muon spectrometer is designed to measure the momentum of particles that escape the calorimeters in the region $|\eta| < 2.7$, and also to trigger on these particles in the region $|\eta| < 2.4$. This is achieved by means of different types of muon chambers optimised for trigger and high-precision measurements. A layout of the muon system is given in Fig. 2.5.

The momentum measurement relies on the bending of the particle trajectory under the effect of the superconducting toroid magnets. The magnetic field is provided by different magnets across $|\eta|$, including the large barrel toroid in the central region, the end-cap magnets inserted into the ends of the barrel toroid, and a combination of both in the intermediate $1.4 < |\eta| < 1.6$ region. The resulting field is mostly orthogonal to the muon trajectories.

The muon chambers form three cylindrical shells around the beam axis in the barrel region, with the third layer being 10 m away from the interaction point. In the transition and end-cap regions, the muon chambers form three wheels perpendicular to the beam. There is a gap at $\eta \sim 0$ to service all the other inner sub-detectors. The momentum of muons is measured in the range $|\eta| < 2.7$ with high precision by Monitored Drift Tube chambers (MDTs). Drift chambers are a type of proportional counters which also include the precise timing measurements of the generated pulses, which provides an accurate determination of the position of the particle. The overall layout is projective. In the forward region, due to the higher muon flux, the inner layer is made of Cathode-Strip Chambers (CSCs). CSCs are multiwire proportional chambers in which the information on the position of the particle is obtained from the orthogonally segmented cathodes. CSCs provide a more robust, high-rate-safe measurement.

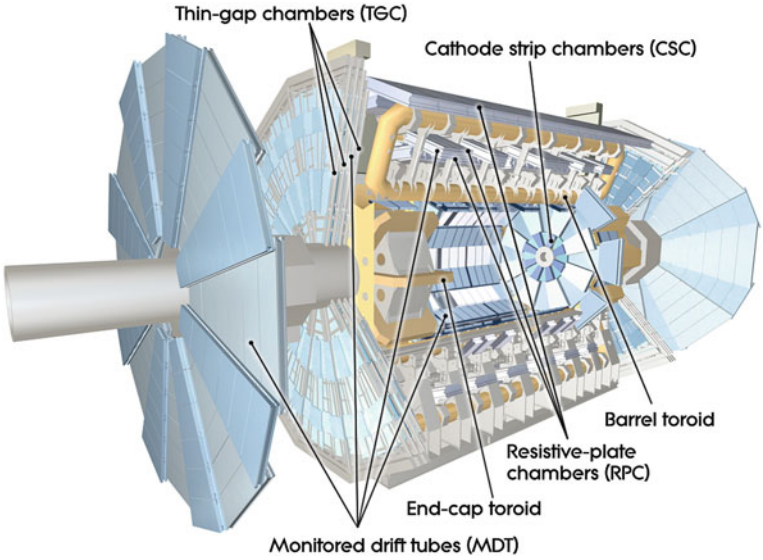

Fig. 2.5 Layout of the ATLAS muon system. From [7]

Complementing the precision-tracking chambers are the trigger chambers, which deliver tracking information within a few tens of nanoseconds. Resistive Plate Chambers (RPCs) cover the barrel region ($|\eta| < 1.05$), structured in three concentric cylindrical layers, and Thin Gap Chambers (TGCs) cover the end-caps ($1.05 < |\eta| < 2.4$). They measure both the η and the ϕ coordinates of the muon tracks. The trigger chambers also provide bunch-crossing identification and complement the measurement of MDTs and CSCs, which can only measure in the bending direction.

2.3 Trigger

The trigger system selects events passing some set of kinematic cuts, typically the transverse momentum of an object, the missing transverse momentum, or some slightly more complex variable. The challenge of the trigger is to reject background without biasing the signal selection, in a short time and at a high rate.

The system is subdivided into three levels. Level 1 (L1) is a hardware-based trigger, which uses coarse detector information from the calorimeter and the muon subsystems (RPCs and TGCs), and produces an answer in less than 2.5 μs. At L1, the objects triggered on include high-p_{T} muons, electrons/photons (which cannot be distinguished at this stage), jets and hadronic τ leptons, and missing transverse momentum. The L1 calorimeter trigger works with approximately 7000 calorimeter trigger trowers of $\Delta\eta \times \Delta\phi \sim 0.1 \times 0.1$ in most cases, or larger at high

pseudorapidities. Geometric information about the objects is kept by the muon and calorimeter trigger processors, and sent to the next level in the form of 'regions of interest' (RoIs) if the event passes the L1 requirements. The input event rate at this stage is 20 MHz (for 50 ns bunch spacing), and the L1 trigger reduces it to a nominal value of 70 kHz.

After being selected by the L1 trigger, events are passed on to the software-based high level trigger (HLT), which has two stages: the Level 2 (L2) trigger and the Event Filter (EF), both of which can already use the full granularity of the data. The L2 trigger increases the level of detail available for the decision by looking at the RoIs defined by the L1. It uses information on coordinates, energy and type of signatures only, in order to minimise the data transfer. It has an average latency of 40 ms, and reduces the event rate to 6 kHz. Finally, successful events pass to the EF, which runs reconstruction algorithms very similar to the offline software. It takes about 4 seconds per event and reduces the event rate down to 400 Hz. The selected events can be recorded for offline analysis.

In order to keep low thresholds, some triggers are prescaled. In prescaled triggers, only a randomly selected fraction of the events passing the trigger cuts are passed onto the next level. The prescale value indicates that only a fraction 1/prescale of the events are accepted. 'Streams' of data are recorded according to whether the events passed one or more of the triggers included in a certain list. Data streams include the 'JetTauEtmiss', 'Egamma' and 'Muon' streams.

A special stream is the 'delayed' stream of data [9]. It is motivated by the realisation that EF triggers are constrained mainly by the processing capacity, and not the storing capabilities. The 'delayed' stream of 8 TeV data recorded additional events at 200 Hz, selecting them with the L1 and L2 triggers, and storing them to be reconstructed after data taking. Softer EF triggers with low or no prescales were run on that fraction of the data.

2.3.1 Jet Triggers

The nominal triggers used in the two analyses presented in this thesis are based solely on jets. The effective trigger efficiency of interest for the offline analysis is a combination of the three stages of the trigger and, in particular, how they reconstruct the jets.

At the L1 level, jet elements are the sum of 2×2 trigger towers in the EM calorimeters and 2×2 towers in the hadronic calorimeters. A threshold is set on the sum of the transverse energy of the calorimeter cells within sliding windows covering 4×4 towers. The sums are compared with the pre-set threshold to decide if the event passes on to the next trigger level.

In the original design of the L2 jet trigger, L1 RoIs were used as seeds to define the region in which more refined calorimeter objects would be studied, using the full calorimeter granularity and running a simple cone-like jet algorithm. However, this approach is insufficient for multi-jet events, since the efficiency of the L1 jet

trigger to identify close-by jets is very low. Full calorimeter reconstruction at the L2 level—with L1-level granularity, to keep within time constraints—was introduced in 2012. The improvement with respect to the L1 full scan is that sophisticated jet algorithms like anti-k_t [10] were run, providing a measurement closer to the offline result. The use of trigger towers at L2 to do a full detector scan is usually abbreviated $L2FS$ [11].

At the EF level, the objects used to build the jets are topological clusters of cells. This improves the resolution with respect to the L2 measurement significantly. Jets are formed using the anti-k_t algorithm using topological clusters from across the whole detector. All the different types of jet algorithm and jet calibration used offline are also available at the EF level. Jet algorithms will be discussed in more detail in Sect. 2.5.4.

2.4 Detector Simulation

In order to interpret the measurements taken by ATLAS, a full simulation of the particle interactions including the effects of the detector is needed. The particles are generated as explained in Sect. 1.3 and then propagated through a simulation of the ATLAS detector performed with the GEANT4 software toolkit [12, 13]. The energy deposits made by outgoing particles in the detector material are recorded with the same format as the standard ATLAS detector readout, and reconstructed using the same software as for real data.

Producing these datasets is computationally expensive, so a lightweight version of the simulation exists that reduces the simulation time by one order of magnitude. The performance improvement is achieved by parameterising the energy profiles of particle showers [14]. This type of detector simulation is called AtlFastII or simply *fast* simulation, as opposed to *full* simulation.

2.5 Object Reconstruction

The electronic signals recorded in the different ATLAS sub-detectors are translated into particles and other physical objects after a series of complex reconstruction, identification and calibration processes. Each type of particle or derived physical object is studied individually. This is done centrally in ATLAS by means of the different performance groups. This section contains a summary of the reconstruction, identification and calibration mechanisms of the different objects relevant for the analyses presented in this thesis.

2.5.1 Tracks

The tracks of charged particles with $p_{\mathrm{T}} > 0.5\,\mathrm{GeV}$ and $|\eta| < 2.5$ can be reconstructed in the ID. The reconstruction process involves a succession of algorithms which define the basic tracker objects; perform the track seeding, fitting, and cleaning; remove fake tracks; extrapolate between the different sub-detectors; and perform a final, global re-fitting to provide the ultimate result.

Tracks are also reconstructed in the muon spectrometer. The procedure has elements in common with the ID track reconstruction process. In this case, track candidates are built from segments, which are straight lines in a single MDT or CSC station, and are joined together by a global track-fitting procedure.

2.5.2 Electrons

Electrons are reconstructed differently depending on which region of the detector they are produced in [15, 16]. In the central region ($|\eta| < 2.5$), a three-step process is performed. First, clusters are built in the EM calorimeter using a sliding-window algorithm of a fixed $\Delta\eta \times \Delta\phi$ size. Then, tracks with $p_{\mathrm{T}} > 0.5\,\mathrm{GeV}$ are extrapolated to the central layer of the EM calorimeter, and matched in η to the EM clusters. An electron candidate is formed when at least one track is matched to the cluster.[3] After reconstruction, the energy of the electron candidate is adjusted by optimising the cluster size in the different calorimeter regions. Other corrections include the energy deposit in front of, outside or beyond the EM calorimeter. The absolute energy scale is determined by exploiting benchmark processes such as $Z \to ee$, $J/\psi \to ee$ or $W \to e\nu$. In the forward region, as there is no tracking information, no distinction is possible between electrons and photons.

Electrons are identified using a set of sequential criteria on different calorimeter, tracking and combined tracking/calorimeter variables, binned in η and E_{T}. Variables used in the identification include shower shapes, hits on particular sections of the detector, or relative energies. Three benchmark selection criteria are set to provide increasing power of background rejection, at the same time that some identification efficiency is lost. They are referred to as the *loose*, *medium* and *tight* quality criteria.

2.5.3 Muons

Muons are reconstructed using a combination of the momentum measurements produced by the ID and the muon spectrometer [17]. Four different techniques are

[3] If a cluster is not matched with a track, it is classified as an unconverted photon candidate.

used to reconstruct muons with energies between 3 GeV and 3 TeV: 'stand-alone' muons, which only use data from the muon spectrometer; 'combined' muons, which combine tracks in the ID and muon spectrometer; 'segment-tagged' muons, which combine a track in the ID with a local track segment in the muon spectrometer (not reconstructed as a track); and 'calorimeter-tagged' muons, formed from a track in the ID and a minimum-ionising-particle-like energy deposit in the calorimeter. The standard class of muons is the combined type. The combined use of these different reconstruction mechanisms ensures that muons are not misreconstructed even if they have low energy or are produced near a transition region.

The momentum scale and resolution of muons are calibrated using large Monte Carlo samples of dimuon resonances, including $J/\psi \to \mu\mu$, $\Upsilon \to \mu\mu$ and $Z \to \mu\mu$.

2.5.4 *Jets*

Jets are narrow and approximately conical bundles of the particles produced by the hadronisation of quarks and gluons in a high-energy physics experiment. This may sound vague; in fact there is no unique jet definition. The different options are classified according to two considerations: what is the set of rules used to group together the particles into a common jet, or *jet algorithm*; and how the momenta of the particles inside the jet are combined, or *recombination scheme*.

Jet reconstruction

Two main types of jet algorithm exist: cone algorithms and sequential-recombination algorithms. The definition of a jet should be such that if an event is modified through soft and collinear radiation, the set of reconstructed jets stays the same. Most variants of cone algorithms are either collinear or infrared unsafe, so they will not be discussed here. In ATLAS sequential-recombination algorithms are used instead, which construct jets via a bottom–up approach in which the sequence of parton splittings is reversed.

The default algorithm used by ATLAS is the anti-k_t algorithm [10]. It is collinear and infrared safe, produces jets of a conical shape, and can be implemented efficiently [18]. The algorithm proceeds as follows. For every pair of particles, the distance measure d_{ij} is defined,

$$d_{ij} = \min\left(\frac{1}{p_{\mathrm{T},i}^2}, \frac{1}{p_{\mathrm{T},j}^2}\right)\frac{\Delta R_{ij}^2}{R^2}, \tag{2.3}$$

where $\Delta R_{ij}^2 = (y_i - y_j)^2 + (\phi_i - \phi_j)^2$, and y_i, ϕ_i and $p_{\mathrm{T},i}$, are respectively the rapidity, azimuth and transverse momentum of particle i. The radius parameter R is set to 0.4 by default. In addition, for every particle a 'beam distance' d_{iB} is also defined,

$$d_{iB} = p_{\mathrm{T}i}^2. \tag{2.4}$$

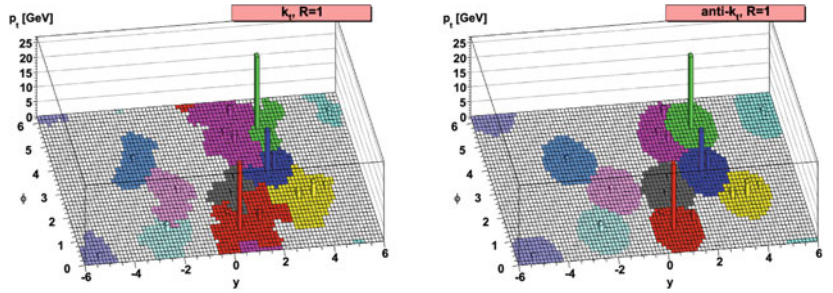

(a) k_{T} algorithm **(b)** anti-k_t algorithm

Fig. 2.6 Example of a simulated parton-level event clustered with the k_{T} (*left*) and the anti-k_t (*right*) algorithms. The shaded regions correspond to the active areas of the jets in y–ϕ space. Figures taken from Ref. [10], where more details are provided

For every particle, its beam distance is compared with all the possible d_{ij}. If the smallest distance is one in the d_{ij} set, then particles i and j are recombined into a new particle. If the smallest distance is d_{iB}, then particle i is defined as a jet and removed from the list of input particles. The distances are recalculated and the procedure repeated until no input particles are left. The anti-k_t algorithm was born from a generalisation of other sequential-recombination algorithms called k_{T} [19, 20] and Cambridge/Aachen [21, 22], both of which produce jets with irregular shapes due to soft radiation. This is illustrated in Fig. 2.6.

The default recombination scheme is to add the four-vectors of the constituent particles, which naturally gives mass to the resulting jet even if the input particles are massless.

Jets in ATLAS

In ATLAS, the inputs to the anti-k_t jet algorithm can be either calorimeter 'topoclusters', tracks, or stable simulated particles in the case of 'truth'-level Monte Carlo simulations. Track jets are not used in this thesis, and truth-level jets will only be used in Chap. 4. Jets can be built with different radii; in this thesis, only $R = 0.4$ jets will be used.

Topoclusters are formed from topologically connected cells in the calorimeter containing an energy deposit above the noise threshold. Topoclusters are calibrated assuming that the energy was deposited by electromagnetic showers by default, and then corrected for the hadronic shower contributions in what is called the 'local cell signal weighting' (LCW) procedure.[4] The procedure includes a classification of the clusters as electromagnetic or hadronic, based mostly on the energy density and longitudinal shower depth.

[4]The ATLAS calorimeter response to electrons is typically 1.3 times higher than the hadron response. This difference is due to energy losses in the hadron case, such as nuclear break-up, spallation and excitation, soft neutrons, neutrinos produced in hadron decays, etc.

Jets are then calibrated to restore their energy scale to that observed in simulated truth particle jets [23]. The procedure consists of several steps. First, pile-up contributions are suppressed using the jet areas pile-up subtraction mechanism [24, 25]. Then, a residual pile-up correction is applied, parametrised as a function of the average number of interactions per bunch crossing, $\langle\mu\rangle$, and the number of primary vertices, N_{PV}. The second stage consists on redirecting the jet in such a way that the origin points to the hard-scatter vertex, instead of the detector vertex. Finally, a correction dependent on p_T and η is applied to take the reconstructed energy of the jet to that of the corresponding truth particle jet as seen in Monte Carlo simulations. A final, residual correction derived from benchmark physics processes measured in data is applied. This correction uses 'in situ' techniques that exploit the balance between jets and well-measured reference objects.

An extra calibration stage was developed at the end of Run 1 to improve the jet energy resolution and reduce the sensitivity of the calibration to the flavour of the jets, without affecting the mean jet energy. The corrections, based on several jet properties —including the number of muon segments behind a jet or the fraction of the energy deposited in different layers of the calorimeter—are applied sequentially. The procedure is known as *global sequential calibration* (GSC) [26], and is applied after all the steps described above.

2.5.5 b-Tagging

Hadronic jets formed from heavy flavour quarks can be identified and tagged with high efficiency using the so-called b-tagging algorithms. The most basic algorithms used in ATLAS are likelihood ratio tests based on the impact parameter (IP3D) or secondary vertices (SV1) [27, 28]. There also exist more sophisticated methods that exploit the topology of the weak decay of b-hadrons, like *JetFitter*. In all cases, the output of the algorithm is a weight computed for every jet in the following way:

$$w_{\text{jet}} = \sum_i w_i = \sum_i \log \frac{b(x_i)}{u(x_i)}, \tag{2.5}$$

where x_i is the discriminating variable, the index i represents either the tracks or the vertices associated with the jet, and $b(x)$ and $u(x)$ are probabilities—obtained by comparing the measured value of x_i with the Monte Carlo expectations—for the b and light jet hypotheses, respectively. Jets are tagged as coming from a b-hadron when their weight is above a certain value, which defines an efficiency working point.

It is still possible to optimise the result (that is, minimise the mistag rate without losing efficiency) by combining the jet weights obtained from different individual algorithms. In particular, the IP3D, SV1 and JetFitter weights are used as inputs to an artificial neural network which produces new weight probabilities for b, c and light-flavour jets, referred to as the MV1 weights.

2.5.6 Missing Transverse Momentum

When the protons collide in ATLAS, their momentum is contained in the longitudinal z direction. By conservation of momentum, it is then expected that the total momentum in the plane transverse to the beam will also be null after the collision. A non-zero global momentum imbalance in the transverse plane can therefore be interpreted as a sign that one or more particles escaped detection. Neutrinos and other hypothetical weakly interacting particles are among the possible sources of missing transverse momentum.

The missing transverse momentum $\mathbf{p}_{\mathrm{T}}^{\mathrm{miss}}$ is computed as the negative vector sum of all the energy deposits in the detector. Its magnitude is usually referred to as 'missing transverse energy', or $E_{\mathrm{T}}^{\mathrm{miss}}$, and it is the most widely used form of the observable.

ATLAS has developed an optimised reconstruction of the $E_{\mathrm{T}}^{\mathrm{miss}}$ which relies partly on all the other calibrated and pile-up suppressed physics objects [29, 30]. The objects are added in a particular order which defines the priorities at the time of removing the overlap between them: electrons with $E_{\mathrm{T}} > 10\,\mathrm{GeV}$, photons with $E_{\mathrm{T}} > 10\,\mathrm{GeV}$, jets with $E_{\mathrm{T}} > 20\,\mathrm{GeV}$ and muons with $E_{\mathrm{T}} > 10\,\mathrm{GeV}$. All the locally calibrated and unmatched clusters within $|\eta| < 4.9$, and any jet with $p_{\mathrm{T}} < 20\,\mathrm{GeV}$ are included in a separate term known as the *soft* term, which is particularly sensitive to pile-up contributions.

$E_{\mathrm{T}}^{\mathrm{miss}}$ can thus be written as

$$(E_{\mathrm{T}}^{\mathrm{miss}})^{\mathrm{RefFinal}} = (E_{\mathrm{T}}^{\mathrm{miss}})^{\mathrm{Electron}} + (E_{\mathrm{T}}^{\mathrm{miss}})^{\mathrm{Gamma}} + (E_{\mathrm{T}}^{\mathrm{miss}})^{\mathrm{Jet}} + (E_{\mathrm{T}}^{\mathrm{miss}})^{\mathrm{Muon}} + (E_{\mathrm{T}}^{\mathrm{miss}})^{\mathrm{Soft}}, \tag{2.6}$$

where RefFinal is the name of the algorithm described above [30]. A consequence of this reconstruction approach is that the mismeasurement of the physics objects may be a source of missing transverse momentum. In these cases it is said that the $E_{\mathrm{T}}^{\mathrm{miss}}$ is *fake*.

The dependence of $E_{\mathrm{T}}^{\mathrm{miss}}$ on calorimeter observables results in its resolution following a stochastic behaviour, which can be approximately parametrised as $\sigma \propto \sqrt{\Sigma E_{\mathrm{T}}}$, where ΣE_{T} is defined as the scalar sum of the transverse energies of reconstructed and calibrated calorimeter objects and of the soft term.[5] The dependence of the $E_{\mathrm{T}}^{\mathrm{miss}}$ resolution on ΣE_{T} has been shown to hold in many situations, including events with different numbers of jets. This fact is the basis of the data-driven multi-jet background determination used in Chap. 3.

[5] The noise and constant terms in the resolution contribute at the very low and very high ΣE_{T} regions, respectively.

References

1. ATLAS Collaboration (2008). The ATLAS experiment at the CERN large hadron collider. *Journal of Instrumentation*, 3.08, S08003.
2. Evans, L., & Bryant, P. (2008). LHC machine. *Journal of Instrumentation*, *3.08*, S08001.
3. Chatrchyan, S., et al. (2008). The CMS experiment at the CERN LHC. *Journal of Instrumentation*, *3*, S08004. doi:10.1088/1748-0221/3/08/S08004.
4. ATLAS Luminosity Public Results. https://twiki.cern.ch/twiki/bin/view/AtlasPublic/LuminosityPublicResults.
5. Doglioni, C. (2012). *Measurement of the inclusive jet cross section with the ATLAS detector at the Large Hadron Collider*. Berlin: Springer.
6. ATLAS Collaboration (2013). Improved luminosity determination in pp collisions at $\sqrt{s} = 7$ TeV using the ATLAS detector at the LHC. *European Physical Journal C*, *73*, 2518. doi:10.1140/epjc/s10052-013-2518-3. arXiv:1302.4393.
7. ATLAS Photos. http://www.atlas.ch/photos/index.html.
8. Olive, K. A., et al. (2014). Review of particle physics. *Chinese Physics C*, *38*(9), 090001.
9. Sfyrla, A. (2013). ATLAS triggering on SUSY in 2012. Tech. rep. ATL-DAQ-PROC-2013-001. Geneva: CERN.
10. Cacciari, M., Salam, G. P., & Soyez, G. (2008). The Anti-k(t) jet clustering algorithm. *Journal of High Energy Physics*, *0804*, 063. doi:10.1088/1126-6708/2008/04/063. arXiv:0802.1189.
11. Rubbo, F. (2013). The design and performance of the ATLAS jet trigger. *European Physical Journal Web of Conferences*, *60*, 20053. doi:10.1051/epjconf/20136020053.
12. Agostinelli, S., et al. (2003). GEANT4: A simulation toolkit. *Nuclear Instruments and Methods in Physics Research Research*, *A506*, 250–303. doi:10.1016/S0168-9002(03)01368-8.
13. ATLAS Collaboration (2010). The ATLAS Simulation Infrastructure. English. *The European Physical Journal C*, *70*(3), 823–874. doi:10.1140/epjc/s10052-010-1429-9. issn: 1434-6044.
14. Richter-Was, E. Poggioli, L. & Froidevaux, D. (1998). ATLFAST 2.0 a fast simulation package for ATLAS. Tech. rep. CERN-ATL-PHYS-98-131.
15. ATLAS Collaboration (2014). Electron reconstruction and identification efficiency measurements with the ATLAS detector using the 2011 LHC proton-proton collision data. *European Physical Journal C*, *74*(7), 2941. doi:10.1140/epjc/s10052-014-2941-0. arXiv:1404.2240.
16. ATLAS Collaboration (2014). Electron and photon energy calibration with the ATLAS detector using LHC Run 1 data. *European Physical Journal C*, *74*(10), 3071. doi:10.1140/epjc/s10052-014-3071-4. arXiv:1407.5063.
17. ATLAS Collaboration (2014). Measurement of the muon reconstruction performance of the ATLAS detector using 2011 and 2012 LHC proton-proton collision data. *European Physical Journal C*, *74*(11), 3130. doi:10.1140/epjc/s10052-014-3130-x. arXiv:1407.3935.
18. Cacciari, M., Salam, G. P., & Soyez, G. Fast Jet user manual. arXiv:1111.6097.
19. Catani, S., et al. (1993). Longitudinally-invariant k⊥-clustering algorithms for hadronhadron collisions. *Nuclear Physics B*, *406*(1), 187–224.
20. Ellis, S. D., & Soper, D. E. (1993). Successive combination jet algorithm for hadron collisions. *Physical Review D*, *48*(7), 3160.
21. Dokshitzer, Y. L., et al. (1997). Better jet clustering algorithms. *Journal of High Energy Physics*, *1997*(08), 001.
22. Wobisch, M. & Wengler, T. (1999). Hadronization corrections to jet cross sections in deep-inelastic scattering. arXiv preprint arXiv:hep-ph/9907280.
23. ATLAS Collaboration (2015). Jet energy measurement and its systematic uncertainty in proton-proton collisions at $\sqrt{s} = 7$ TeV with the ATLAS detector. *The European Physical Journal C*, *75*(1), 17. doi:10.1140/epjc/s10052-014-3190-y. issn: 1434-6044.
24. Cacciari, M., & Salam, G. P. (2008). Pileup subtraction using jet areas. *Physics Letters B*, *659*, 119. doi:10.1016/j.physletb.2007.09.077. arXiv:0707.1378.
25. ATLAS Collaboration (2013). Pile-up subtraction and suppression for jets in ATLAS. Tech. rep. ATLAS-CONF-2013-083. Geneva: CERN.

26. Batista, S. & Begel, M. et al. (2014). Global sequential calibration with the ATLAS detector in proton-proton collisions at $\sqrt{s} = 8$ TeV with ATLAS 2012 data. Tech. rep. ATL-COM-PHYS-2014-753. Geneva: CERN.
27. ATLAS Collaboration. Expected performance of the ATLAS experiment - detector, trigger and physics. CERN-OPEN-2008-020. arXiv:0901.0512.
28. ATLAS Collaboration (2011). Commissioning of the ATLAS high-performance b-tagging algorithms in the 7 TeV collision data. Tech. rep. ATLAS-CONF-2011-102. Geneva: CERN.
29. ATLAS Collaboration (2013). Performance of missing transverse momentum reconstruction in ATLAS studied in proton-proton collisions recorded in 2012 at 8 TeV. Tech. rep. ATLAS-CONF-2013-082. Geneva: CERN.
30. ATLAS Collaboration (2012). Performance of missing transverse momentum reconstruction in proton-proton collisions at 7 TeV with ATLAS. *European Physical Journal C*, *72*, 1844. doi:10.1140/epjc/s10052-011-1844-6. arXiv:1108.5602.

http://www.springer.com/978-3-319-43460-5

High Jet Multiplicity Physics at the LHC

Crispin Ortuzar, M.

2016, XXII, 177 p. 95 illus., 62 illus. in color., Hardcover
ISBN: 978-3-319-43460-5